

Decoupling Molybdenum Disulfide from its Substrate by Cesium Intercalation

Roberto Sant,^{†,‡,¶} Simone Lisi,[‡] Van Dung Nguyen,[‡] Estelle Mazaleyrat,[§] Ana
Cristina Gómez Herrero,[‡] Olivier Geaymond,[‡] Valérie Guisset,[‡] Philippe David,[‡]
Alain Marty,^{||} Matthieu Jamet,^{||} Claude Chapelier,[⊥] Laurence Magaud,[‡] Yannick
J. Dappe,[#] Marco Bianchi,[@] Philip Hofmann,[@] Gilles Renaud,[†] and Johann
Coraux^{*,‡}

[†]*Univ. Grenoble Alpes, CEA, IRIG/DEPHY/MEM, 38000 Grenoble, France*

[‡]*Univ. Grenoble Alpes, CNRS, Grenoble INP, Institut NEEL, 38000 Grenoble, France*

[¶]*ESRF, The European Synchrotron, 38043 Grenoble, France*

[§]*Univ. Grenoble Alpes, CEA, IRIG/DEPHY/PHELIQS, 38000 Grenoble, France*

^{||}*Univ. Grenoble Alpes, CEA, CNRS, Grenoble INP, IRIG/DEPHY/SpinTec, 38000
Grenoble, France*

[⊥]*Univ. Grenoble Alpes, CEA, IRIG, IRIG/DEPHY/PHELIQS, 38000 Grenoble, France*

[#]*SPEC, CEA, CNRS, Université Paris-Saclay, CEA Saclay 91191 Gif-sur-Yvette Cedex,
France*

[@]*Department of Physics and Astronomy, Interdisciplinary Nanoscience Center (iNANO),
Aarhus University, 8000 Aarhus C, Denmark*

E-mail: johann.coraux@neel.cnrs.fr

Abstract

Intercalation of alkali atoms within the lamellar transition metal dichalcogenides is a possible route toward a new generation of batteries. It is also a way to induce structural phase transitions authorizing the realization of optical and electrical switches in this class of materials. The process of intercalation has been mostly studied in three-dimensional dichalcogenide films. Here, we address the case of a single-layer of molybdenum disulfide (MoS_2), deposited on a gold substrate, and intercalated with cesium (Cs) in ultra-clean conditions (ultrahigh vacuum). We show that intercalation decouples MoS_2 from its substrate. We reveal electron transfer from Cs to MoS_2 , relative changes in the energy of the valence band maxima, and electronic disorder induced by structural disorder in the intercalated Cs layer. Besides, we find an abnormal lattice expansion of MoS_2 , which we relate to immediate vicinity of Cs. Intercalation is thermally activated, and so is the reverse process of de-intercalation. Our work opens the route to a microscopic understanding of a process of relevance in several possible future technologies, and shows a way to manipulate the properties of two-dimensional dichalcogenides by "under-cover" functionalization.

Introduction

The interest for transition metal dichalcogenide single-layers, initially spurred by the bright light emission found in molybdenum disulfide (MoS_2)^{1,2} and the achievement of electrostatic switching of electrical conduction in MoS_2 ,³ has revived activities devoted to the synthesis of these materials. Efforts to elaborate them with a structural quality similar to the one obtained in mechanically exfoliated samples with bottom-up approaches – chemical vapour deposition,^{4–7} chalcogenation of metal surfaces,^{8–10} or molecular beam epitaxy, standard¹¹ or reactive under H_2S atmosphere^{12–14} – are ongoing. Both chalcogenation and reactive molecular beam epitaxy usually require a metallic substrate. As-prepared samples are hence not suited to the study of some of the key properties of the material, *e.g.* those related to exci-

tons which become very short-lived due to the immediate vicinity of a metallic (substrate) charge reservoir, and electrical transport properties which are shunt by the conductive substrate. Besides, in the prototypical case of Au(111) as a substrate, MoS₂ does not retain the properties of the isolated material. Significant interaction between the electronic bands of MoS₂ and Au(111) was indeed detected¹⁵ and the existence of a moiré pattern was found to induce a nanometer-scale modulation of this interaction.¹⁶

One way to alter this interaction is to "lift" MoS₂ from its surface. Actually, such lifting occurs spontaneously, across regions spanning typically a nanometer, when MoS₂ overhangs on Ångström-deep vacancy islands of the substrate.¹⁷ Effective lifting may be achieved using an alternative strategy, namely by intercalating a layer of a species decoupling MoS₂ from its substrate. This strategy, which allowed to obtain quasi-free-standing graphene^{18,19} (another two-dimensional material), has been explored recently with single-layer WS₂,²⁰ but not with single-layer MoS₂ so far, to our knowledge.

On the contrary, intercalation of thicker transition metal dichalcogenides has been thoroughly investigated. Much like with graphite, a rich variety of systems with modulated structure in the direction perpendicular to the basal plane can be formed this way.²¹ Using layers of alkali atoms, molecules, or transition metals as intercalants, unique properties including superconductivity and (anti)ferromagnetism have been found.²¹ The ability to store (release) alkali atoms by intercalation (de-intercalation) also makes transition metal dichalcogenides possible electrode materials, both as cathode²² and anode,²³⁻²⁵ for Li-ion batteries. Electrodonor intercalants promote a structural phase transition from a semiconducting phase to a metallic one,²⁶⁻³⁵ with potential applications in data storage and reconfigurable electrical circuitry.

Here, we report on the intercalation and de-intercalation of the alkali cesium (Cs) atoms. Unlike all works addressing in-solution intercalation of bulk-like transition metal dichalcogenide layers, the focus of our work is on single-layer MoS₂ flakes, prepared on Au(111), and (de)intercalated under ultrahigh vacuum conditions. We find that the process of intercala-

tion is thermally activated, being completed after few tens of minutes at a temperature of 550 K. Above 850 K, deintercalation is efficient and completed within a few tens of minutes. Intercalated cesium forms a Cs monolayer with an ill-ordered structure compatible with a $(\sqrt{3} \times \sqrt{3})R30^\circ$ reconstruction with respect to Au(111). We reveal electron transfer from Cs to MoS₂, modifications of the relative positions of the valence band maxima in MoS₂, and electronic disorder induced by structural disorder in the intercalated layer. Upon intercalation, MoS₂ is lifted, and adopts an unusually large lattice parameter. Our analysis combines scanning tunneling microscopy (STM), reflection high-energy electron diffraction (RHEED), grazing incidence X-ray diffraction (GIXRD), reflectivity (XRR), X-ray photoelectron spectroscopy (XPS), and angle-resolved photoemission spectroscopy (ARPES) all performed under ultrahigh vacuum, in some cases *in operando* during intercalation. Further insights are brought by density functional theory (DFT) calculations.

Methods

Three ultrahigh vacuum systems were used for our experiments. A first one is coupled to the X-ray synchrotron beam delivered at the BM32 beamline of the ESRF. It has a base pressure of 3×10^{-10} mbar and is equipped with a quartz micro-balance and a RHEED apparatus. The second one, at Institut Néel (Grenoble), with a base pressure of 2×10^{-10} mbar, is part of a larger ultrahigh vacuum system comprising a STM, a RHEED apparatus, and a quartz microbalance. The samples were prepared in each system before being investigated by RHEED, STM, GIXRD, and XRR. Temperatures were measured with a pyrometer in both systems. Note that the pyrometers and the chamber configurations are different in the two systems, which implies a plausible variability (~ 50 K) in the measurements, and suggests caution when comparing these measurements. The third ultrahigh vacuum system is installed at the SGM-3 endstation³⁶ of the ASTRID2 synchrotron radiation source (Aarhus); it includes one chamber (base pressure 10^{-10} mbar) devoted to ARPES and XPS

measurements, and two other chambers (base pressures, 4×10^{-10} mbar) comprising a STM. All three ultrahigh vacuum systems are equipped with a Cs evaporator. MoS₂/Au(111) was prepared in Grenoble and transported in atmospheric conditions to Aarhus where it was degassed in ultrahigh vacuum at 500 K. There, temperatures were measured using a K type thermocouple fixed on the rear side of the Au (111) crystal. The cleanliness of the surface was confirmed with STM and photoelectron spectroscopy.

Single-crystals bought from Surface Preparation Laboratory and Mateck were prepared under ultrahigh vacuum by repeated cycles of room temperature sputtering with 0.8-1 keV Ar⁺ ions and annealing to 900 K. Surface cleanliness was checked with STM imaging and RHEED, both revealing a well-developed herringbone reconstruction. Molybdenum was evaporated using a high-purity rod heated by electron-beam bombardment, at a rate of 0.02 monolayer/min in the ultrahigh vacuum chamber coupled to the X-ray beam and in the ultrahigh vacuum chamber coupled to the STM, respectively (one monolayer referring to the surface coverage of a single-layer MoS₂ on Au(111)). This rate was determined with both a quartz microbalance and STM. For introduction of H₂S in the ultrahigh vacuum chambers, we used an automatic injection system by VEGATEC that supplies H₂S via pneumatic valves (chamber coupled to the X-ray beam), and a leak-valve (chamber coupled to the STM). The latter system comprises large copper parts. Their surface was saturated by maintaining a pressure of 10^{-6} mbar of H₂S for 30 min. Without this treatment, residual gas analysis revealed that H₂S was prominently decomposed before even reaching the sample surface, which prevented MoS₂ growth.

Cesium was deposited under ultrahigh vacuum by resistive heating of a high purity Cs dispenser (SAES Getter). Assessing the deposited Cs dose is not a straightforward task. Cesium dose measurements, using a quartz microbalance for instance, are seldom reported. Exceptions include low temperature measurements;³⁷ in contrast, our room temperature measurements were inconclusive. Alternative calibration methods were hence needed. In the ultrahigh vacuum system where STM imaging was performed, graphene growth on Ir(111) is

operative. Cesium deposition in this system leads to its intercalation between graphene and Ir(111) in a sequence of well-crystallized phases readily detected with electron diffraction.³⁸ At fixed current flowing the Cs dispenser (6.5 A) we hence determined the deposition time required for the onset of a $(\sqrt{3} \times \sqrt{3})R30^\circ$ Cs reconstruction relative to the graphene lattice, which corresponds to a well-defined Cs density. Using this calibration, we deposited Cs in two steps, each at room temperature followed by a 500 K annealing, with a total nominal Cs quantity equivalent to 0.7 Cs atoms per Au atom on the surface. In the ultrahigh vacuum system where XPS and ARPES data were acquired, a second calibration method was used. Cesium was deposited (5.7 A current) for a given time at room temperature onto Au(111), and the Cs density was assessed by comparing the area under the Cs peaks and Au surface $4f$ components in XPS, assuming that Cs is in the form of a flat sub-monolayer deposit. With this calibration at hand, we then deposited Cs in two steps, each at room temperature followed by 550 K annealing, corresponding nominally to 0.3 and 0.6 Cs atoms per Au atom on the surface. In the third ultrahigh vacuum system, installed at the BM32 beamline, we could not use any of these two methods. We hence decided to deposit a large excess of Cs, using a high current flowing the Cs dispenser (7.2 A) and large deposition times, each of 30 min. There also we deposited Cs sequentially, in three steps, each at room temperature followed by a 500 K annealing.

Diffraction measurements were performed at European Synchrotron Radiation Facility using a z -axis diffractometer installed at the BM32 CRG/IF beamline and optimized for grazing incidence surface X-ray diffraction. The experimental energy was set at 11.8 keV, below the Au L_{III} absorption edge. The incident angle was set to 0.24° , slightly below the critical angle for total external reflection, to enhance the signal from MoS_2 while minimizing the background. The diffraction signal was acquired with a Maxipix two-dimensional detector (256×1288 pixels, each of size $55 \mu\text{m}$).

The XRR spectra were processed with PyRod (home-made software for surface diffraction 2D data treatment). Data were integrated in reciprocal space and the profiles were extracted

as a function of the modulus of the scattering vector perpendicular to the surface (Q_{\perp}). Corrections to this integrated intensity were applied for beam polarization, surface active area and gaussian beam profile. Correction for beam refraction at interfaces were used to calculate Q_{\perp} inside the sample. The ANA-ROD software³⁹ was used for modeling the surface structure of the samples and fitting the XRR data.

The STM data we show were acquired in Grenoble with an Omicron STM-1 apparatus, at room temperature under ultrahigh vacuum, in a dedicated chamber with a base pressure of 5×10^{-11} mbar. At the SGM-3 endstation, an Aarhus STM was used to check the sample quality after Cs deposition, which gave consistent results with those obtained in Grenoble.

ARPES and XPS measurements were performed at the SGM-3 end station of the ASTRID2 synchrotron radiation source.³⁶ The ARPES and XPS data were collected at room temperature at photon energies of 49 eV and 130 eV respectively. The energy and angular resolutions were better than 20 meV and 0.2° respectively.

Structural relaxations as well as electronic structure determination have been performed using DFT. The DFT localized-orbital molecular-dynamics code as implemented in `Fireball`^{40–42} has been used to optimize the $\text{MoS}_2/\text{Au}(111)$ and the $\text{MoS}_2/\text{Cs}/\text{Au}(111)$ structures or to determine their corresponding electronic properties. Standard previously used basis sets have been considered for Mo, S and Au,⁴³ and an *sp* basis set with cut-off radii of 6.8 (in atomic units), has been considered for Cs. A hexagonal slab of 7×7 Au atoms with five layers in the *xy* plane, and a topmost 6×6 MoS_2 have been used to model the $\text{MoS}_2/\text{Au}(111)$ interface. This configuration has been optimized until the forces become less than $0.1 \text{ eV}/\text{\AA}$. The bottom two Au layers were fixed to simulate the Au bulk for the $\text{MoS}_2/\text{Au}(111)$ interface. The $\text{MoS}_2/\text{Cs}/\text{Au}(111)$ system, with a $(\sqrt{3} \times \sqrt{3})R30^{\circ}$ Cs reconstruction on Au(111) requires a large supercell to be treated. In this systems, the atomic positions were fixed to the average values derived from the analysis of the XRR data. We have used a set of 32 *k*-points in the plane for self-consistency and density of states calculations.

Results and Discussion

Single-layer MoS₂ flakes were grown following the procedure described by Grønberg *et al.*⁴⁴ In short, the clean Au(111) surface was exposed to a partial pressure of H₂S ($P_{\text{H}_2\text{S}}$) introduced in the ultrahigh vacuum systems, then molybdenum was deposited on the surface in presence of H₂S, and the sample was annealed to 900 K without the Mo atomic beam but still in presence of H₂S. This sequence was repeated several times to adjust the surface coverage with MoS₂. In the two ultrahigh vacuum chambers where MoS₂ was grown, we used $P_{\text{H}_2\text{S}} = 10^{-5}$ and 10^{-6} mbar respectively. Figure 1a-d shows the typical diffraction patterns and morphology of the surface after growth. The MoS₂ flakes exhibit straight edges,⁴⁵ have an extension of the order of several 10 nm; in between the flakes the herringbone reconstruction of the bare Au(111) is visible. The fraction of the surface covered with MoS₂ was $70\pm 15\%$, $28\pm 5\%$, and $25\pm 15\%$ (as determined from the nominal amount of Mo deposited on the surface, or with STM whenever possible) for the samples studied with GIXRD/XRR, STM, and XPS/ARPES, respectively. Our STM observations are consistent with those in previous reports.^{13,44}

Structure of MoS₂ single-layer islands on Au(111). A pronounced pattern, with 3.17 ± 0.01 nm periodicity, is visible on the MoS₂ flakes presented in Figure 1c,d. This pattern arises from the lattice mismatch between MoS₂ and the substrate, and is described with an analogy to the optical moiré effect.¹³ Careful analysis of atomically-resolved STM images and their Fourier transform (Figure 1b) allows to determine the size of the moiré unit cell. For the example shown in Figure 1, we find that the highest symmetry Au(111) and MoS₂ crystallographic directions are precisely aligned, and that the unit cell corresponds to the coincidence of 10 MoS₂ unit cells onto 11 Au(111) unit cells (10×11), consistent with a recent report.¹⁴

This moiré unit cell is varying from one MoS₂ island to another. The average reciprocal space lattice vector associated to the moiré is directly inferred from RHEED (Figure 1a) and GIXRD (Figure 1e,f) data by measuring the relative positions of the moiré or MoS₂ peaks

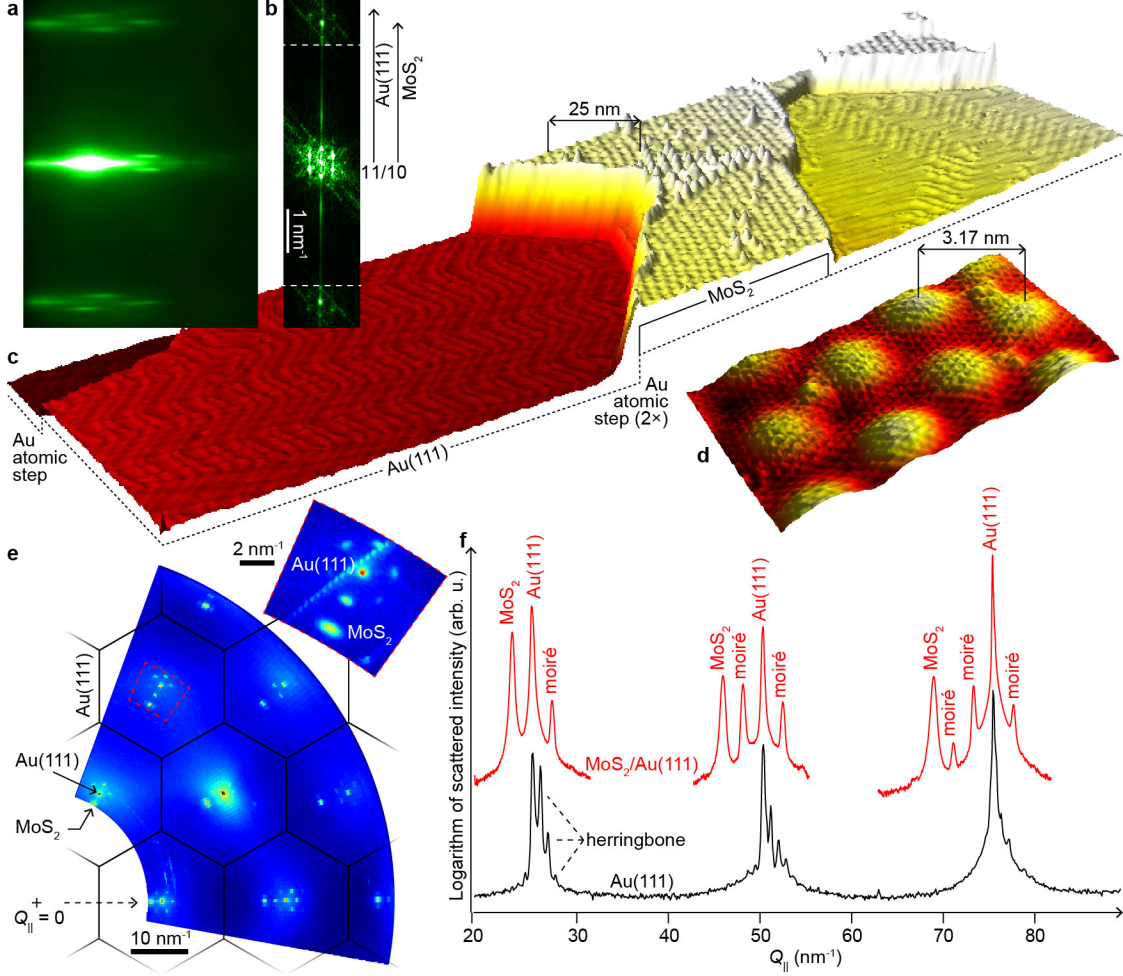


Figure 1: Single layer MoS₂ islands prepared on Au(111). (a) RHEED diffractogram (17 keV) along the [1 $\bar{1}$ 0] azimuth. On either side of the most intense central specular streak, MoS₂ and moiré streaks are observed, the latter ones corresponding to the shortest vertical distances on the pattern. (b) Fast Fourier transform of an atomically resolved STM image (the contrast and brightness below and above the dotted line, at the vicinity of the MoS₂ spots, have been enhanced). The reciprocal space vectors corresponding to the Au(111) and MoS₂ lattices are highlighted with two arrows, whose length ratio is 11/10. (c) Three-dimensional view of a STM topograph (2 nA, -2 V) of single-layer MoS₂ islands formed on Au(111), with the herringbone reconstruction of the latter visible. Defects in the moiré appear as high bumps. (d) Three-dimensional view of an atomically-resolved STM topograph (0.81 nA, -1.93 V) of the moiré lattice between Au(111) and MoS₂. (e) In-plane cut of the reciprocal lattice, as measured with X-rays. Top right: higher-resolution measurement of the area marked with a dotted frame. (f) Radial scan of the X-ray scattered intensity in the direction shown with a dotted arrow in e, as a function of the modulus of the in-plane scattering vector Q_{\parallel} for Au(111) with and without single-layer MoS₂ islands on top.

with respect to the Au(111) peaks, to be $1.884 \pm 0.001 \text{ nm}^{-1}$.

The full-width at half maximum of the MoS₂ peaks in a radial direction (Figure 1f)

increases from $0.32 \pm 0.05 \text{ nm}^{-1}$ to $0.51 \pm 0.05 \text{ nm}^{-1}$ from first to third order. This corresponds to a domain size of about 20 nm and a distribution of in-plane lattice parameter of typically 0.6%.⁴⁶ Strikingly, the domain size is here smaller than the value of several 10 nm corresponding to the flake size that we determined by visual inspection of STM images. This difference simply shows that the flakes are not single-crystal, and actually consist each of (smaller) single-crystal grains. As discussed in the Supporting Information (SI), we indeed frequently observe linear defects within the flakes, at the boundary between laterally-shifted domains within the flake (see Figure S1). Our interpretation is that at each of the several steps of the MoS₂ cyclic preparation, new MoS₂ islands nucleate, grow, and coalesce with pre-existing ones – no lattice re-organisation occurs that would eliminate the linear defect (so-called out-of-phase grain boundaries) to yield large single-crystal flakes.

To model the structure of MoS₂ and learn more about the out-of-plane structure of the material, we use DFT calculations taking van der Waals interactions into account. For that purpose, we choose an unsheared moiré unit cell with 6 MoS₂ units matching 7 Au(111) surface units. This (6×7) coincidence lattice is not the (10×11) observed experimentally. Our choice is however legitimate since in our DFT calculations, the lattice structure optimization are performed at 0 K (while the measurements are performed at 300 K), a temperature at which the lattice parameters of bulk Au(111) (0.2883 nm) and MoS₂ (0.3293 nm) are in a different ratio (1.14, *i.e.* close to 7/6) than those measured for bulk compounds at room temperature (0.2884 nm and 0.3167 nm, ratio = 1.10 = 11/10, see Ref. 47). The DFT commensurate structure is a realistic approximant of the experimental unit cell and we expect to capture the physics of interaction. This structure is also computationally more demanding than the (1×1) and $(\sqrt{13} \times \sqrt{13})R13.9^\circ$ commensurate approximants used so far.¹⁵

Figure 2a shows a top-view of the minimum-energy structure of MoS₂ on Au(111) that has been optimised with the DFT calculations. Periodic lattice distortions are found in both MoS₂ and Au(111). The in-plane projection of the distortions of the topmost Au(111) layer

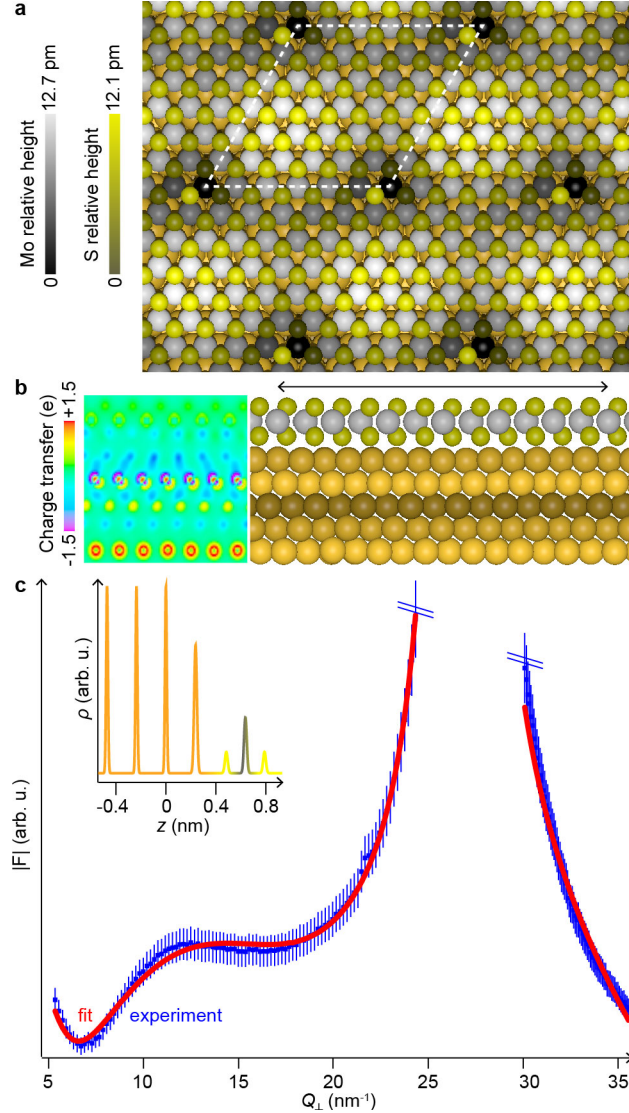


Figure 2: Nature of the bonding for MoS₂ onto Au(111). (a) Top-view of the optimized geometry found with DFT calculations. The Mo (S) atoms are sketched with gray (yellow) balls, whose shade codes the variation of height. The rhombus highlights the commensurate (6×7) moiré unit cell employed for the calculations. (b) Cross-section of the charge transferred between atoms, along an edge of the rhombus, and of the atomic structure, along the long diagonal of the rhombus (of length indicated with a double arrow), calculated with DFT. The different layers of the Au(111) substrate are coloured according to the sequence of ABC planes in a *fcc* stack. (c) Experimental structure factor F modulus (XRR, blue dots) as function of the modulus of the out-of-plane scattering vector Q_{\perp} , and best fit to the experimental data (red curve). Inset: Electronic density profile versus out-of-plane coordinate (z), corresponding to the best fit.

and of the Mo layer are better visualised in Figure S2, where they have been amplified. They range from typically 1 to 8 pm (Au), and 1 to 4 pm (Mo). In another epitaxial two-

dimensional material, graphene, smaller (~ 1 pm) and larger (~ 20 pm) distortions have been reported on Ir(111) (Ref. 48) and Ru(0001) (Ref. 49) substrates. In the former system no or very weak moiré peaks were observed while they were clearly observed in the latter.⁵⁰ Our observation of intense moiré diffraction peaks in MoS₂/Au(111), and the fact that among these peaks, those located closer to the Au(111) diffraction peaks are those with higher intensity (Figure 1f), are consistent with significant distortions in the Au lattice.

Regarding the out-of-plane structure (Figure 2b), according to the DFT calculations the average distance between the topmost Au plane and the closest S plane, $d_{\text{Au-S}}$, amounts 0.252 nm, while the average distance between the Mo and top (bottom) S planes is $d_{\text{Mo-S}} = 0.153$ nm (0.156 nm). The $d_{\text{Au-S}}$ interlayer value is smaller than the 0.312 nm interlayer distance value found in our DFT calculations for an infinite multilayer of 2H-MoS₂, where the interplanar interactions are of van der Waals type. We note that the $d_{\text{Mo-S}}$ values, on the contrary, are very similar to the one obtained with multilayer of 2H-MoS₂. The values of $d_{\text{Au-S}}$ and $d_{\text{Mo-S}}$ are modulated along the moiré pattern, by only few 10 pm and few 1 pm respectively. This suggests that the apparent height modulations of typically 100 pm observed with STM in relation with the moiré pattern, are essentially of electronic nature.

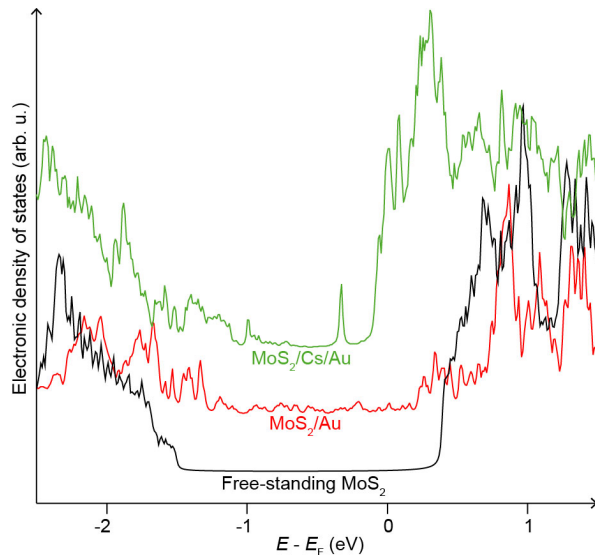


Figure 3: Electronic density of states derived from DFT calculations for free-standing MoS₂, MoS₂ on Au(111) in a (6×7) coincidence lattice, and MoS₂ on Au(111) with an intercalated $(\sqrt{3} \times \sqrt{3})R30^\circ$ Cs layer.

The short $d_{\text{Au-S}}$ values shows that strong Au-S bonds exist in the system, and this is confirmed by the DFT analysis of the charge transfer at the interface between MoS₂ and Au(111) (Figure 2b). Within the unit cell, a spatial modulation of the charge held by the S atoms in the bottom layer and by the Au top layers is observed. This is a signature of a spatially varying interaction between MoS₂ and Au(111), which is expected when hybridization between the electronic orbitals of MoS₂ and Au(111) occurs locally within the moiré, where the atoms belonging to each material are positioned properly. The bottom S layers has a deficit of electrons (blue shades in Figure 2b), while the Mo and top S layers rather have an excess of electrons (green to light-green shades in Figure 2b). This is consistent with the electronic density of states, also calculated with DFT, which shows that the bottom of the conduction band is down-shifted by about 160 meV compared to the case of free-standing MoS₂ (Figure 3, see also discussion in the SI and Figure S3). Overall the DFT analysis indicates that the MoS₂ single layer on Au(111) is slight electron-doped.

We now confront the DFT analysis to the experimental analysis of the out-of-plane structure via XRR. The modulus of the Fourier transform of the total electronic density of the system along the out-of-plane direction (Figure 2c) is obtained by taking the square root of the XRR data. In between the (000) and (111) crystallographic reflections of Au(111) (modulus of the out-of-plane scattering vector Q_{\perp} , 0 nm⁻¹ and 26.68 nm⁻¹), we observe a bump in the reflectivity. Qualitatively, the local reflectivity minima correspond to destructive interferences between the X-ray waves scattered by the Au(111) lattice and by the MoS₂ layer, perpendicular to the surface. The distance between the minima is related to the distances between the layers (it decreases when the interlayer distance increases, and *vice versa*).

We performed a more quantitative analysis by calculating the structure factor of an atomic model of MoS₂/Au(111), and refining the values of the free structural parameters to fit the calculation to the experimental data, using the ANA-ROD code.³⁹ In short (see Figure S4a and Table S1 for details), we assume two regions that scatter incoherently, one with the bare Au(111) surface, the other with MoS₂/Au(111), consistent with the partial coverage

of the surface with MoS₂. We disregard the above-discussed (weak) periodic distortion, to limit the number of free parameters and thus to ensure a reliable fit. The topmost Au (111) atomic plane is let free to move in the z direction, to account for surface relaxation. The above-defined $d_{\text{Au-S}}$ and $d_{\text{Mo-S}}$ distances are also free parameters for the fit. Finally, the roughness of the surface is modeled within the so-called β model,⁵¹ with β as another free parameter. We obtain a very good fit to the experimental data (Figure 2c) for the electronic density profile shown in the inset of Figure 2c, that yields refined values of $d_{\text{Au-S}} = 0.243 \pm 0.025$ nm and $d_{\text{Mo-S}} = 0.153 \pm 0.022$ nm. These values are in very good agreement with the outcome of the DFT calculations.

Cesium deposition and intercalation of Cs underneath MoS₂. STM was performed after the nominal deposition of 0.7 Cs per Au surface atom and 500 K annealing. On MoS₂-free regions Cs atoms form a pattern of ~ 5 nm-long nanosticks, some bunching across several 1 nm to several 10 nm, and having different orientations on the surface, also detected in the Fourier transform of the images (Figure 4a,b). The strong structural disorder evident on the STM image explains the absence of a Cs-related diffraction signature at room temperature in RHEED and GIXRD. Considering the observed local periodicity, we propose two possible atomic structures for the Cs nanosticks (Figure 4c).

We observe two kinds of MoS₂-covered regions (Figure 4a,d,e). Part of the MoS₂ has a similar height as the Cs-covered Au(111) surface, and exhibits a moiré pattern. The majority ($\sim 85\%$) of MoS₂ islands however has a higher apparent height and exhibits no moiré pattern. A reasonable interpretation is that the latter islands are intercalated with a Cs layer, while the former islands are not. This intercalated layer is not directly accessible to STM measurements. We observe a nanoscale pattern of lines oriented along the three highest-symmetry directions of Au(111) and MoS₂ (120° orientations). This pattern may be related to that observed in another intercalated two-dimensional-material-on-metal system, graphene/Bi/Ir(111).⁵² There, the pattern was interpreted as a network of dislocations in the intercalant's lattice, the lines corresponding to the boundaries between intercalated domains

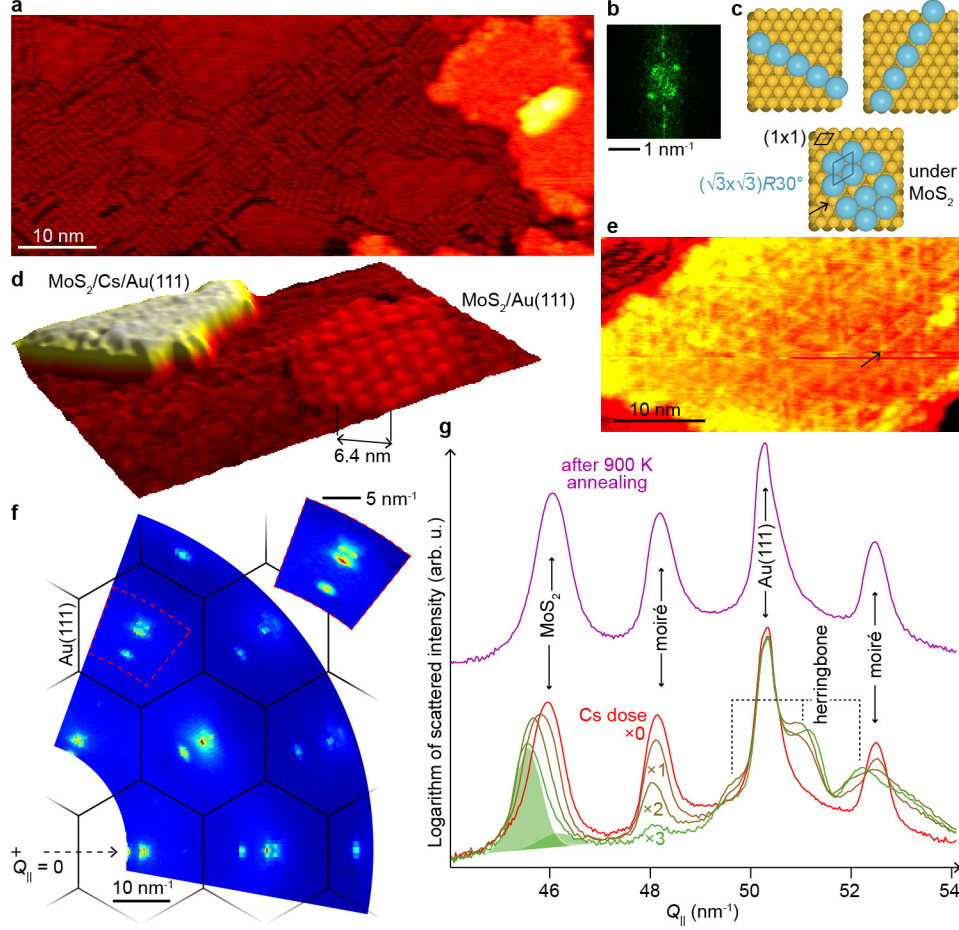


Figure 4: Structural changes in MoS₂ upon Cs intercalation. (a) STM view (0.2 nA, -2 V) revealing Cs nanosticks on Au(111) after deposition (nominally 0.7 Cs atoms per Au surface atom) at room temperature and annealing to 500 K. (b) Fast Fourier transform of a region with nanosticks. (c) Cartoons of the possible structures for the Cs nanosticks and of the $(\sqrt{3} \times \sqrt{3})R30^\circ$ Cs phase intercalated under MoS₂. (d) Three-dimensional view of a STM topograph (0.65 nA, -0.5 V) showing MoS₂ islands with and without intercalated Cs. (e) Close-up STM view (0.2 nA, -2 V) of a MoS₂ island revealing a pattern of lines. (f) In-plane reciprocal map measured with X-rays after the deposition of three excess Cs doses and 550 K annealing. Top-right: high-resolution measurement in the area marked with a red-dashed frame. (g) Radial scan of the X-ray scattered intensity versus the in-plane momentum transfer Q_{\parallel} . The bottom four scans have been measured each after the additional deposition of an excess Cs dose and subsequent annealing at 550 K, while the top scan has been measured after the final Cs deposit/annealing followed by an annealing at 900 K. For the largest dose the two components (green areas) used to fit the MoS₂ peak are shown.

being shifted by a fraction of the lattice vector(s) of the intercalant's lattice (Figure 4c).

The disappearance of the moiré pattern observed in STM is corroborated by GIXRD measurements. After three cycles of deposition of a large Cs excess followed by 550 K

annealing, the reciprocal space lattice of the sample shows no discernable moiré signals (compare Figures 4f,1e). In fact, the reduction of the moiré signals rather occurs after than before each 550 K annealing (Figure 4g). The process is hence thermally-activated, indicative of kinetically limitations.

Concomitantly to the vanishing of the moiré signal, the GIXRD data reveal that the diffraction signal associated to MoS₂ progressively shows two components, the one at lower scattering vector modulus corresponding to an expansion of the lattice (Figure 4g). The latter component may be assigned to intercalated islands, while the other corresponds to pristine, still-unintercalated MoS₂ islands on Au. This suggests that intercalation proceeds sequentially, island by island. In other words, the limiting kinetic step in the intercalation process corresponds to the opening of an intercalation channel, for instance a point defect or the unbinding of (part of) the flake edges from the substrate. Once this channel is opened, mass transport underneath the flake is presumably very efficient at the several-10 nm-scale considered here. At the end of the three deposition+annealing cycles, close to 100% of the islands are intercalated (note that the intensity scale in Figure 4g is logarithmic).

The GIXRD data show a decrease in intensity and an angular broadening of the diffraction peaks as the Cs dose increases (compare Figures 4f,1e), which both point to increased disorder in the form of in-plane strains and mosaic spread. Conversely, we observe a resurgence of the diffraction signals of the Au reconstruction (Figure 4g), suggesting that the Au-MoS₂ interaction has been suppressed.

Strain induced by intercalation. In the absence of a significant hybridization between MoS₂ and Au orbitals, the MoS₂ is no more strongly pinned on the substrate lattice. Consistent with this view, the in-plane lattice parameter of MoS₂ is found to change (the MoS₂ diffraction peak is shifted to lower momentum transfer values, Figure 4g), *i.e.* the MoS₂ lattice is no longer strained by its substrate. More precisely, a 0.9% lattice expansion is observed at 300 K compared to the value found in bulk MoS₂.⁴⁷

Several effects may explain this expansion. First, MoS₂ is grown at 900 K, a temperature

at which the ratio of lattice parameters for MoS₂ and Au(111) is expected to be precisely 1.10,^{47,53,54} *i.e.* precisely the 11/10 ratio determined experimentally after the sample is cooled down to room temperature. This is yet another indication that prior to intercalation MoS₂ is strongly bonded on its substrate, with an epitaxial relationship that is unchanged between growth temperature and room temperature. In the opposite extreme case, if during cool down MoS₂ were free to compress according to its own natural thermal compression (and not that of the Au(111) substrate, which is slightly larger), the lattice parameter of MoS₂ would be slightly larger, by $\sim 0.2\%$.^{47,53,54} This is the maximum expansion we expect due to the suppression of the strong bonding between MoS₂ and Au upon intercalation. This effect hence only accounts for a small fraction of the observed 0.9% expansion.

What is the origin of the remaining $\sim 0.7\%$ expansion? A structural phase transition (1H to 1T or 1T') is expected upon electron doping,⁵⁵ and Cs, a well-known electro-donor species, might indeed donate the required amount of charges to MoS₂. The 1T phase is not expected to have a significantly different lattice constant (a marginally shorter lattice constant has even been predicted⁵⁶) while the 1T' phase should.⁵⁷ However our diffraction measurements do not detect a doubling of the MoS₂ unit cell that would be expected for this phase. There is another reason why an increasing amount of alkali atoms in the vicinity of MoS₂ could actually lead to an increased lattice constant. In the related system of potassium inserted in between MoS₂ layers, DFT calculations predicted a significant lattice expansion. There, the role of the increased charge density within the Mo-S bonds was invoked.⁵⁸ Our own DFT calculations with free-standing MoS₂ (this is a rough, yet reasonable description of MoS₂ decoupled from Au(111) by intercalation) predict that adding about 0.1 electrons per MoS₂ unit cell (to mimic the charge transfer associated to intercalation) yields a lattice expansion by typically several 0.1%.

We again examine the structure of the sample perpendicular to the surface. While for pristine MoS₂/Au(111), the XRR spectrum exhibited essentially one intensity rebound (Figure 2c), after Cs deposition and annealing at least four rebounds ($\sim 8, 16, 22, 35 \text{ nm}^{-1}$) are

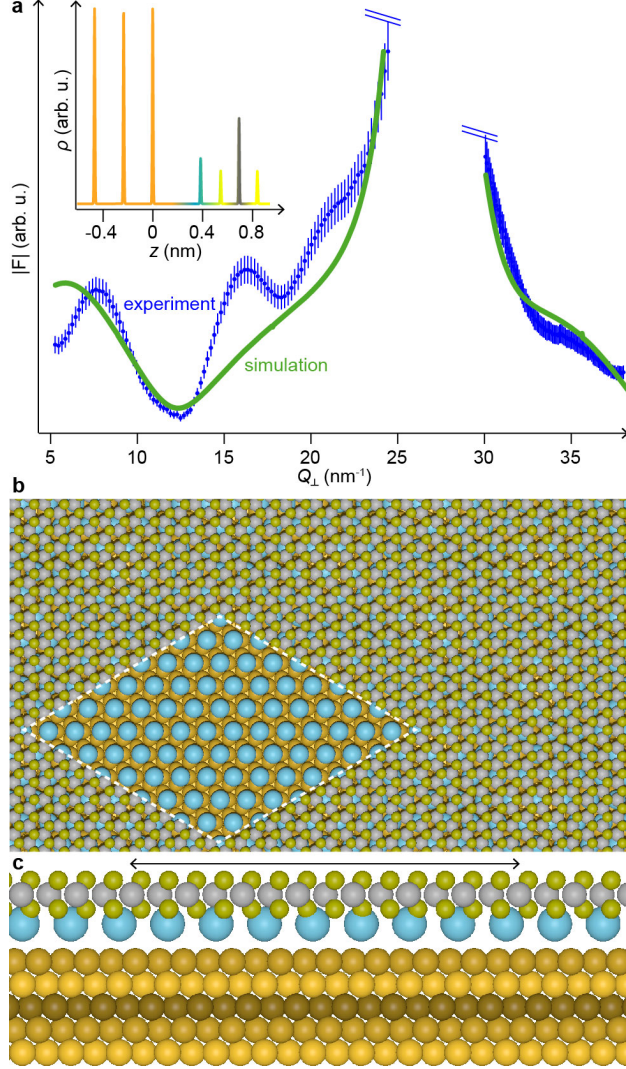


Figure 5: Nature of the structure and bonding after Cs intercalation. (a) Experimental structure factor F modulus (XRR, blue dots) as function of Q_{\perp} after three deposits of an excess Cs + 550 K annealing, and best simulation to the experimental data (green curve). Inset: Corresponding electronic density profile along z . (b) Top-view of the geometry optimized from the XRR analysis and used for DFT calculations. The Mo (S) atoms are sketched with gray (yellow) balls, whose shade codes the variation of height. The Cs atoms are sketched with cyan balls. The rhombus highlights the commensurate $(6 \times 7) (\sqrt{30} \times \sqrt{30}) R30^{\circ}$ moiré unit cell. Within the area of the rhombus, we do not show the MoS₂ atoms to display the underlying $(\sqrt{30} \times \sqrt{30}) R30^{\circ}$ Cs layer. (c) Cross-section, along the long diagonal of the rhombus, of the atomic structure, along the long diagonal of the rhombus, deduced from the analysis of the XRR data. The Au(111) layers are coloured according to the fcc sequence of ABC planes.

observed (Figure 5a). The distance between the extrema decreasing with increasing interplanar distances, this new observation is consistent with an increased $d_{\text{Au-S}}$ distance, compared

to the case of MoS₂/Au(111). This is precisely what is expected if a Cs layer is intercalated between MoS₂ and Au(111). To test this interpretation, we have adjusted $d_{\text{Au-S}}$ (and the distance $d_{\text{Au-Cs}}$ between the Cs layer and the Au topmost plane; see SI for further details). Given the large atomic radius of Cs, we expect a low-density Cs phase. Our STM analysis directly confirms that on MoS₂-free regions (Figure 4a-c), the shortest Cs-Cs distances are indeed large, matching the second nearest neighbour Au-Au distance on the surface, *i.e.* 0.499 nm. Two-dimensional materials tend to alter the organisation of intercalant as shown in the case of graphene,⁵⁹ hence an even lower density in the intercalated Cs layer, as *e.g.* in a (2×2) phase, cannot be excluded *a priori*. However our simulations agree less with the XRR data in the case of such a low-density phase, suggesting that a denser phase, for instance a $(\sqrt{3} \times \sqrt{3})R30^\circ$ reconstruction, provides a more realistic description of the system. The best match of our model to the experimental data is obtained for $d_{\text{Au-S}} = 0.551$ nm and $d_{\text{Au-Cs}} = 0.389$ nm (see Table S2 for details). The $d_{\text{Au-S}}$ value is increased by about 0.308 nm compared to the case without intercalated Cs. The increase is close, but 0.07 nm less than that observed in Cs-intercalated multilayer MoS₂.⁶⁰

Figure 5a obviously shows that this model is too simple to faithfully reproduce *all* the features in the experimental XRR data. In particular, between 15 nm^{-1} and 25 nm^{-1} , the model only accounts for the baseline of the experimental spectrum, and does not produce the two marked intensity rebounds. As discussed more into details in the SI (see Figure S5 and Table S3 for another simulation with a more advanced model), what is not captured by our simple model is the multilayer thickness of the Cs layer on bare Au(111) (unlike under MoS₂, where it is intercalated as a single-layer). Multilayer Cs is expected there because we chose to deposit a large excess of Cs on the surface for the samples characterized with XRR (and GIXRD), due to the lack of reliable calibration of the Cs deposition rate in the corresponding ultrahigh vacuum chamber (see *Methods*). On MoS₂, long-ranged Cs surface diffusion and Cs desorption are instead expected already at room temperature to result in (i) low-surface-density Cs clusters, and (ii) mass transport of Cs out of the MoS₂ surface,

towards MoS₂-free regions and vacuum. 550 K annealing will further promote this tendency, and strongly reduce the Cs cluster density on MoS₂.

Thermal de-intercalation. As already mentioned, increasing the temperature promotes intercalation of Cs underneath the MoS₂ flakes, which points to a kinetic barrier to intercalation (*e.g.* for passing through defects and/or for creating defects later acting as intercalation pathways). To further improve the efficiency of intercalation it is tempting to further increase temperature. Above about 800 K however, another key process is activated: the moiré signal re-appears in GIXRD, the MoS₂ peak shifts back to its initial position (Figure 4g), and the XRR spectrum strongly resembles that of as-deposited MoS₂/Au(111). In fact, after 900 K annealing, the reciprocal lattice of the sample is very similar to that of the pristine sample, *i.e.* Cs has been de-intercalated. How is this occurring? An XPS analysis (see SI) reveals that a fraction of Cs adatoms penetrates the Au crystal already at room temperature, even more so at 550 K (Figure S6) and at 850 K. In addition to this process, at 850 K Cs atoms may have a non-negligible probability to cross the energy barrier for diffusing outside the MoS₂ islands, and to subsequently desorb to vacuum.

Electronic effects of Cs intercalation. We expect that intercalation of Cs has strong influence on the electronic properties of MoS₂. We start with experimental measurements, with ARPES, of energy-momentum cuts in the electronic band structure along K Γ KM in reciprocal space, first with the case of as-grown MoS₂/Au(111). The valence band of MoS₂ (whose maxima are highlighted with horizontal lines in Figure 6), with a characteristic 130 meV spin-orbit splitting at K point, is clearly seen (Figure 6a). Its maxima at Γ and K points lie 1.67 eV and 1.35 eV respectively below the Fermi level, while the conduction band minimum is above the Fermi level, consistent with a previous report.¹⁵

After the deposition of nominally 0.3 Cs atom per surface Au atom, and thermally-induced intercalation the ARPES energy-momentum cuts (Figure 6b) and energy distribution curves (EDCs, Figure S7) show that the MoS₂ valence band maximum at the Γ and K points shift down, by 20 meV. No additional electronic band is observed that would corre-

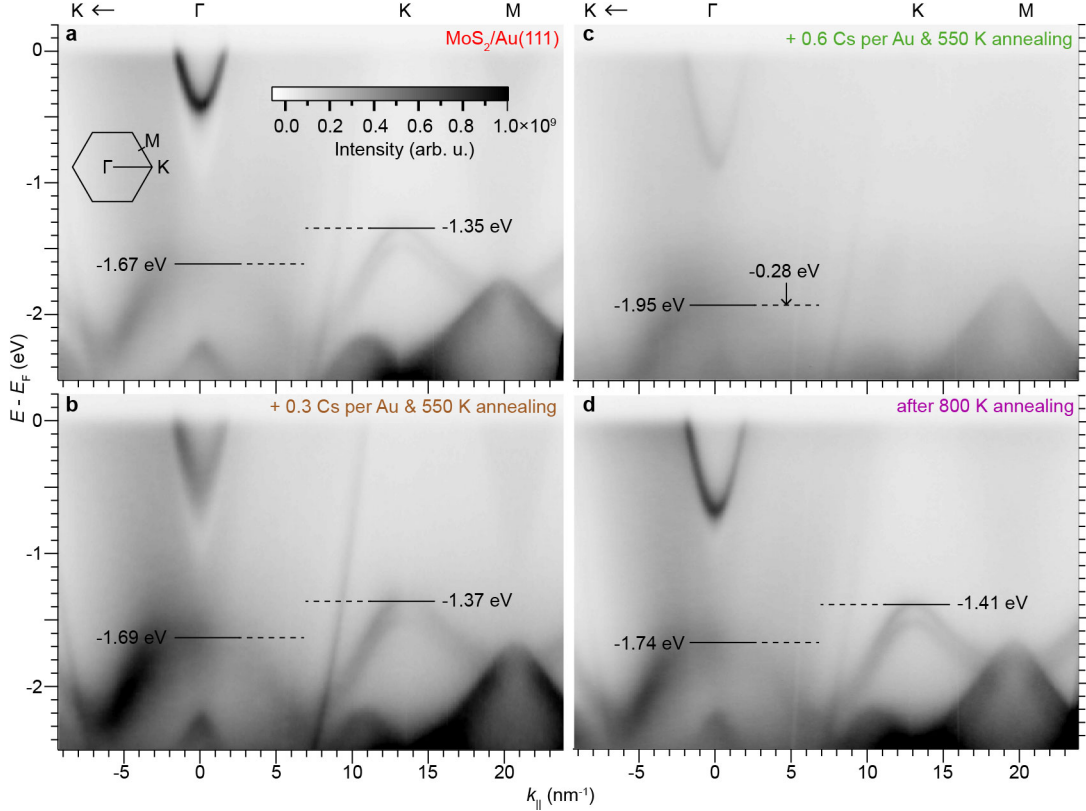


Figure 6: Electronic modifications upon intercalation. Photoemission intensity along high-symmetry reciprocal space directions (MΓKM, see inset), with a 49 eV photon energy, for (a) pristine MoS₂/Au(111), and (b,c) the same sample exposed to an increasing Cs dose +0.3 and +0.6 Cs atoms per Au surface atom (followed by 550 K annealing), and (d) eventually annealed to 850 K. The black lines mark the positions of the valence band extrema before/after Cs intercalation.

spond to Cs. Tripling the Cs dose yields stronger changes in the electronic band structure of MoS₂ (Figures 6c,S7): the MoS₂ valence band maximum at Γ point further shifts down, by as much as 280 meV. The photoemission signal corresponding to the MoS₂ valence band at the vicinity of the K point becomes weaker and broader. Inspection of the EDCs (Figure S7) is required to detect a down-shift, of about 100 meV.

The Au(111) surface state at the Γ point, close to the Fermi level, is observed before and all along the Cs deposition/annealing procedure (Figure 6). The signature of this surface state is naturally related to the occurrence of the Au(111) herringbone reconstruction observed in STM in between MoS₂ islands (Figure 1c) and with GIXRD after Cs deposition/annealing (Figure 4g). This indicates that Cs is weakly adsorbed on Au, hence not altering the sensitive

Au(111) reconstruction/surface state. We note that as the Cs dose increases, the surface state shifts down in binding energy (Figure 6a-c). Shifts of this kind have been observed for Na adsorbed on Cu(111),⁶¹ and have been explained by a polarization-induced filling of the surface state.⁶²

These observations are reminiscent of a previous study that explored charge transfers induced by potassium (K) atoms in MoS₂/Au(111).⁶³ In the two studies, the most prominent effects seem to be a non-rigid down-shift of the electronic band structure, with different magnitude at Γ and K points. The shifts are of the same order of magnitude with potassium and cesium, suggesting charge transfers (the Fermi level is changed) in the same range. The origin of the shifts can be qualitatively rationalised by inspecting the projection of the electronic states on the different orbitals in the system, which has been calculated by DFT for a (1 \times 1) approximate model for MoS₂ on Au(111).¹⁵ The spin-orbit-split MoS₂ valence band close to K point is expected to be primarily of Mo $d_{x^2-y^2} + d_{xy}$ character and the fact that it is not significantly shifted upon intercalation suggests that it is not related to a possible hybridization with the substrate's electronic band (the hybridization would be strongly affected by intercalation), which seems reasonable for these in-plane MoS₂ orbitals. In the energy range explored in Figure 6, at Γ point the stronger contribution to the valence band stems from Mo $d_{z^2} + d_{yz} + d_{xz}$ out-of-plane orbitals, and these bands are indeed expected to be involved in the hybridization and charge transfers with the substrate or the alkali atoms, consistent with our observations (Figure 6).

The broadening of the valence band at K point after Cs intercalation points to a significant disorder in the system. This is consistent with our STM observations of a disordered nanoscaled pattern for Cs in this case (Figure 4c,e). Strikingly, annealing the sample to 850 K allows to recover a well-defined valence band at K point (compare Figure 6a,d), consistent with the deintercalation process also evident in GIXRD (Figure 4g) and XRR, which we interpret as a consequence of Cs diffusion into bulk Au or Cs desorption from the surface. This is also an indication that the source of electronic disorder was indeed extrinsic to the

MoS₂, *i.e.* due to the intercalant, and not intrinsic to MoS₂, *i.e.* due to the creation of defects in the dichalcogenide single-layer.

Our ARPES observation can be rationalised in the framework of a simplified DFT calculation scheme. Minimising the structure of the MoS₂/Cs($\sqrt{3} \times \sqrt{3}$)R30°/Au(111) system would require to consider a large commensurate calculation supercell comprising about 1,100 atoms (in a ($\sqrt{3} \times \sqrt{3}$)R30°, and not a (1×1), moiré unit cell), among which high- Z number ones. This is computationally prohibitive, and we prefer, instead, to analyse the electronic density of states for the values of $d_{\text{Au-Cs}} = 0.389$ nm and $d_{\text{Au-S}} = 0.551$ nm (see structural model represented in Figures 5b,c) which we derived from the analysis of the XRR data. Keeping in mind the limitations of the latter analysis, we also considered another set of $d_{\text{Au-Cs}}$ and $d_{\text{Au-S}}$ values, for which the Cs layer is further from (closer to) the MoS₂ layer (Au(111) surface), see SI for details.

Figure 3 compares the electronic density of states in the presence of the intercalated layer ($d_{\text{Au-Cs}} = 0.389$ nm, $d_{\text{Au-S}} = 0.551$ nm) to the case of MoS₂/Au(111) and the case of isolated MoS₂. The bottom of the conduction band is further down-shifted, by about 320 meV, relative to the case of MoS₂/Au(111), which is indicative of a strong electron doping of MoS₂, consistent with our ARPES observations. This tendency is robust and is also predicted for different $d_{\text{Au-Cs}}$ and $d_{\text{Au-S}}$ values (Figure S3). The level of electronic doping seems comparable to the one that we expect for an isolated MoS₂ layer, with three Cs atoms adsorbed per (10 × 10) MoS₂ unit cells (Figure S3).

Except for one marked peak (-330 meV) that we ascribe to an interfacial Au/Cs state, within about 600 meV below the bottom of the conduction band, the DFT calculations predict few in-gap states than for MoS₂/Au(111). Below this energy range more in-gap states are predicted, at least for $d_{\text{Au-Cs}} = 0.389$ nm and $d_{\text{Au-S}} = 0.551$ nm. Their occurrence is however highly dependent on the distance between the bottom S layer and the Cs layer, as shown for a calculation performed with another set of $d_{\text{Au-Cs}}$ and $d_{\text{Au-S}}$ values (Figure S3).

Conclusions

We showed that starting from MoS₂ flakes strongly coupled to the Au(111) substrate, with a short spacing and a substantial nanorippling, Cs intercalation lifts the flakes and flattens them. The process is thermally activated. De-intercalation is also thermally activated, but at higher temperatures. We found that Cs, which is intercalated in the form of an atomic layer whose density is consistent with a $(\sqrt{3} \times \sqrt{3})R30^\circ$ reconstruction on Au(111), substantially dopes MoS₂ with electrons, and that this doping is a possible origin for a $\sim 1\%$ expansion of the atomic lattice of MoS₂ parallel to the surface. The interaction with the Cs layer is associated with relative changes in the energy of the valence band maxima and to electronic disorder presumably related to the structural disorder in Cs.

Our work opens new perspectives towards the manipulation of two-dimensional transition metal dichalcogenides. Similarly to in-solution strategies,²⁹ intercalation could be exploited on MoS₂/Au(111) to facilitate the exfoliation of nanoscale flakes¹² or full layers.¹⁴ Demonstrating further control on electronic or hole doping of MoS₂ with intercalated electro-donor or electro-acceptor species is another exciting goal. A number of species, to be intercalated with varying doses, are relevant here, among the vast catalog of alkali atoms, transition metals, and molecules. Finally, as extensively demonstrated with bulk compounds in the past, intercalation opens new doors to achieve a variety of two-dimensional phases, structural ones, magnetic ones, and even superconducting ones.

Acknowledgement

R.S. acknowledges financial support by Nanosciences Foundation. This work was supported by the 2DTransformers project under the OH-RISQUE program (ANR-14-OHRI-0004), J2D (ANR-15-CE24-0017) and ORGANISO (ANR-15-CE09-0017) projects of Agence Nationale de la Recherche (ANR), by the French state funds Equipex ANR-11-EQPX-0010, ANR-10-LABX-51-01 (Labex LANEF of "Programme d'Investissements d'Avenir"), ANR-15-IDEX-

02, and by the Région Rhône Alpes (ARC6 program) and the Labex LANEF. The was also supported by VILLUM FONDEN via the Centre of Excellence for Dirac Materials (Grant No. 11744). We thank Tao Zhou for his kind support.

Supporting Information Available

The following files are available free of charge.

Supporting information comprises additional STM data showing defects in MoS₂, the results of DFT calculations on deformations in MoS₂ and its substrate, energy distribution ARPES curves, and a DFT analysis of the the influence of an intercalated AuCs alloy on the electronic properties of MoS₂.

References

- (1) Splendiani, A.; Sun, L.; Zhang, Y.; Li, T.; Kim, J.; Chim, C.-Y.; Galli, G.; Wang, F. Emerging Photoluminescence in Monolayer MoS₂. *Nano Lett.* **2010**, *10*, 1271–1275.
- (2) Mak, K. F.; Lee, C.; Hone, J.; Shan, J.; Heinz, T. F. Atomically Thin MoS₂: A New Direct-Gap Semiconductor. *Phys. Rev. Lett.* **2010**, *105*, 136805.
- (3) Radisavljevic, B.; Radenovic, A.; Brivio, J.; Giacometti, i. V.; Kis, A. Single-Layer MoS₂ Transistors. *Nat. Nanotech.* **2011**, *6*, 147.
- (4) Zhan, Y.; Liu, Z.; Najmaei, S.; Ajayan, P. M.; Lou, J. Large-Area Vapor-Phase Growth and Characterization of MoS₂ Atomic Layers on a SiO₂ Substrate. *Small* **2012**, *8*, 966–971.
- (5) Liu, K.-K.; Zhang, W.; Lee, Y.-H.; Lin, Y.-C.; Chang, M.-T.; Su, C.-Y.; Chang, C.-S.; Li, H.; Shi, Y.; Zhang, H. et al. Growth of Large-Area and Highly Crystalline MoS₂ Thin Layers on Insulating substrates. *Nano Lett.* **2012**, *12*, 1538–1544.

- (6) Lee, Y.-H.; Zhang, X.-Q.; Zhang, W.; Chang, M.-T.; Lin, C.-T.; Chang, K.-D.; Yu, Y.-C.; Wang, J. T.-W.; Chang, C.-S.; Li, L.-J. et al. Synthesis of Large-Area MoS₂ Atomic Layers with Chemical Vapor Deposition. *Adv. Mater.* **2012**, *24*, 2320–2325.
- (7) Eichfeld, S. M.; Hossain, L.; Lin, Y.-C.; Piasecki, A. F.; Kupp, B.; Birdwell, A. G.; Burke, R. A.; Lu, N.; Peng, X.; Li, J. et al. Highly Scalable, Atomically Thin WSe₂ Grown via Metal-Organic Chemical Vapor Deposition. *ACS Nano* **2015**, *9*, 2080–2087.
- (8) Kim, D.; Sun, D.; Lu, W.; Cheng, Z.; Zhu, Y.; Le, D.; Rahman, T. S.; Bartels, L. Toward the Growth of an Aligned Single-Layer MoS₂ Film. *Langmuir* **2011**, *27*, 11650–11653.
- (9) Orofeo, C. M.; Suzuki, S.; Sekine, Y.; Hibino, H. Scalable Synthesis of Layer-Controlled WS₂ and MoS₂ Sheets by Sulfurization of Thin Metal Films. *Appl. Phys. Lett.* **2014**, *105*, 083112.
- (10) Wang, Y.; Li, L.; Yao, W.; Song, S.; Sun, J.; Pan, J.; Ren, X.; Li, C.; Okunishi, E.; Wang, Y.-Q. et al. Monolayer PtSe₂, a New Semiconducting Transition-Metal Dichalcogenide, Epitaxially Grown by Direct Selenization of Pt. *Nano Lett.* **2015**, *15*, 4013–4018.
- (11) Ugeda, M. M.; Bradley, A. J.; Shi, S.-F.; Felipe, H.; Zhang, Y.; Qiu, D. Y.; Ruan, W.; Mo, S.-K.; Hussain, Z.; Shen, Z.-X. et al. Giant Bandgap Renormalization and Excitonic Effects in a Monolayer Transition Metal Dichalcogenide Semiconductor. *Nat. Mater.* **2014**, *13*, 1091–1095.
- (12) Helveg, S.; Lauritsen, J. V.; Lægsgaard, E.; Stensgaard, I.; Nørskov, J. K.; Clausen, B.; Topsøe, H.; Besenbacher, F. Atomic-Scale Structure of Single-Layer MoS₂ Nanoclusters. *Phys. Rev. Lett.* **2000**, *84*, 951.
- (13) Sørensen, S. G.; Füchtbauer, H. G.; Tuxen, A. K.; Walton, A. S.; Lauritsen, J. V. Structure and Electronic Properties of In Situ Synthesized Single-Layer MoS₂ on a Gold Surface. *ACS Nano* **2014**, *8*, 6788–6796.

- (14) Bana, H.; Travaglia, E.; Bignardi, L.; Lacovig, P.; Sanders, C. E.; Dendzik, M.; Michiardi, M.; Bianchi, M.; Lizzit, D.; Presel, F. et al. Epitaxial Growth of Single-Orientation High-Quality MoS₂ Monolayers. *2D Mater.* **2018**, *5*, 035012.
- (15) Bruix, A.; Miwa, J. A.; Hauptmann, N.; Wegner, D.; Ulstrup, S.; Grønberg, S. S.; Sanders, C. E.; Dendzik, M.; Čabo, A. G.; Bianchi, M. et al. Single-Layer MoS₂ on Au(111): Band Gap Renormalization and Substrate Interaction. *Phys. Rev. B* **2016**, *93*, 165422.
- (16) Krane, N.; Lotze, C.; Franke, K. J. Moiré Structure of MoS₂ on Au(111): Local Structural and Electronic Properties. *Surf. Sci.* **2018**, *678*, 136–142.
- (17) Krane, N.; Lotze, C.; Läger, J. M.; Reecht, G.; Franke, K. J. Electronic Structure and Luminescence of Quasi-Freestanding MoS₂ Nanopatches on Au(111). *Nano Lett.* **2016**, *16*, 5163–5168.
- (18) Varykhalov, A.; Sánchez-Barriga, J.; Shikin, A.; Biswas, C.; Vescovo, E.; Rybkin, A.; Marchenko, D.; Rader, O. Electronic and Magnetic Properties of Quasifreestanding Graphene on Ni. *Phys. Rev. Lett.* **2008**, *101*, 157601.
- (19) Riedl, C.; Coletti, C.; Iwasaki, T.; Zakharov, A.; Starke, U. Quasi-Free-Standing Epitaxial Graphene on SiC Obtained by Hydrogen Intercalation. *Phys. Rev. Lett.* **2009**, *103*, 246804.
- (20) Mahatha, S. K.; Dendzik, M.; Sanders, C. E.; Michiardi, M.; Bianchi, M.; Miwa, J. A.; Hofmann, P. Quasi-Free-Standing Single-Layer WS₂ Achieved by Intercalation. *Phys. Rev. Materials* **2018**, *2*, 124001.
- (21) Friend, R.; Yoffe, A. Electronic Properties of Intercalation Complexes of the Transition Metal Dichalcogenides. *Adv. Phys.* **1987**, *36*, 1–94.

- (22) Murugan, A. V.; Quintin, M.; Delville, M.-H.; Campet, G.; Gopinath, C. S.; Vijayamohan, K. Exfoliation-Induced Nanoribbon Formation of Poly(3,4-Ethylene Dioxythiophene) PEDOT Between MoS₂ Layers as Cathode Material for Lithium Batteries. *J. Power Sources* **2006**, *156*, 615–619.
- (23) Whittingham, M. S. Electrical Energy Storage and Intercalation Chemistry. *Science* **1976**, *192*, 1126–1127.
- (24) Feng, C.; Ma, J.; Li, H.; Zeng, R.; Guo, Z.; Liu, H. Synthesis of Molybdenum Disulfide (MoS₂) for Lithium Ion Battery Applications. *Mater. Res. Bull.* **2009**, *44*, 1811–1815.
- (25) Li, Z.; Jiang, K.; Khan, F.; Goswami, A.; Liu, J.; Passian, A.; Thundat, T. Anomalous Interfacial Stress Generation During Sodium Intercalation/Extraction in MoS₂ Thin-Film Anodes. *Sci. Adv.* **2019**, *5*, eaav2820.
- (26) Py, M.; Haering, R. Structural Destabilization Induced by Lithium Intercalation in MoS₂ and Related Compounds. *Canadian J. Phys.* **1983**, *61*, 76–84.
- (27) Wypych, F.; Schöllhorn, R. 1T-MoS₂, a New Metallic Modification of Molybdenum Disulfide. *J. Chem. Soc. Chem. Comm.* **1992**, 1386–1388.
- (28) Heising, J.; Kanatzidis, M. G. Structure of Restacked MoS₂ and WS₂ Elucidated by Electron Crystallography. *J. Am. Chem. Soc.* **1999**, *121*, 638–643.
- (29) Eda, G.; Yamaguchi, H.; Voiry, D.; Fujita, T.; Chen, M.; Chhowalla, M. Photoluminescence from Chemically Exfoliated MoS₂. *Nano Lett.* **2011**, *11*, 5111–5116.
- (30) Wang, Y.; Ou, J. Z.; Balendhran, S.; Chrimes, A. F.; Mortazavi, M.; Yao, D. D.; Field, M. R.; Latham, K.; Bansal, V.; Friend, J. R. et al. Electrochemical Control of Photoluminescence in Two-Dimensional MoS₂ Nanoflakes. *ACS Nano* **2013**, *7*, 10083–10093.

- (31) Wang, X.; Shen, X.; Wang, Z.; Yu, R.; Chen, L. Atomic-Scale Clarification of Structural Transition of MoS₂ Upon Sodium Intercalation. *ACS Nano* **2014**, *8*, 11394–11400.
- (32) Fan, X.; Xu, P.; Zhou, D.; Sun, Y.; Li, Y. C.; Nguyen, M. A. T.; Terrones, M.; Mallouk, T. E. Fast and Efficient Preparation of Exfoliated 2H-MoS₂ Nanosheets by Sonication-Assisted Lithium Intercalation and Infrared Laser-Induced 1T to 2H Phase Reversion. *Nano Lett.* **2015**, *15*, 5956–5960.
- (33) Guo, Y.; Sun, D.; Ouyang, B.; Raja, A.; Song, J.; Heinz, T. F.; Brus, L. E. Probing the Dynamics of the Metallic-to-Semiconducting Structural Phase Transformation in MoS₂ Crystals. *Nano Lett.* **2015**, *15*, 5081–5088.
- (34) Xiong, F.; Wang, H.; Liu, X.; Sun, J.; Brongersma, M.; Pop, E.; Cui, Y. Li Intercalation in MoS₂: In Situ Observation of its Dynamics and Tuning Optical and Electrical Properties. *Nano Lett.* **2015**, *15*, 6777–6784.
- (35) Ahmad, M.; Müller, E.; Habenicht, C.; Schuster, R.; Knupfer, M.; Büchner, B. Semiconductor-to-Metal Transition in the Bulk of WSe₂ Upon Potassium Intercalation. *J Physics: Condens. Matter.* **2017**, *29*, 165502.
- (36) Hoffmann, S.; Søndergaard, C.; Schultz, C.; Li, Z.; Hofmann, P. An Undulator-Based Spherical Grating Monochromator Beamline for Angle-Resolved Photoemission Spectroscopy. *Nucl. Instrum. Methods Phys. Res. Sect. A* **2004**, *523*, 441–453.
- (37) Taborek, P.; Rutledge, J. Novel Wetting Behavior of ⁴He on Cesium. *Phys. Rev. Lett.* **1992**, *68*, 2184.
- (38) Petrović, M.; Rakić, I. Š.; Runte, S.; Busse, C.; Sadowski, J.; Lazić, P.; Pletikosić, I.; Pan, Z.-H.; Milun, M.; Pervan, P. et al. The Mechanism of Caesium Intercalation of Graphene. *Nat. Commun.* **2013**, *4*, 1–8.

- (39) Vlieg, E. ROD: a Program for Surface X-Ray Crystallography. *J. Appl. Cryst.* **2000**, *33*, 401–405.
- (40) Lewis, J. P.; Jelínek, P.; Ortega, J.; Demkov, A. A.; Trabada, D. G.; Haycock, B.; Wang, H.; Adams, G.; Tomfohr, J. K.; Abad, E. et al. Advances and Applications in the FIREBALL Ab Initio Tight-Binding Molecular-Dynamics Formalism. *Phys. Stat. Sol. b* **2011**, *248*, 1989–2007.
- (41) Jelínek, P.; Wang, H.; Lewis, J. P.; Sankey, O. F.; Ortega, J. Multicenter Approach to the Exchange-Correlation Interactions in Ab Initio Tight-Binding Methods. *Phys. Rev. B* **2005**, *71*, 235101.
- (42) Sankey, O. F.; Niklewski, D. J. Ab Initio Multicenter Tight-Binding Model for Molecular-Dynamics Simulations and Other Applications in Covalent Systems. *Phys. Rev. B* **1989**, *40*, 3979.
- (43) González, C.; Biel, B.; Dappe, Y. J. Theoretical Characterisation of Point Defects on a MoS₂ Monolayer by Scanning Tunnelling Microscopy. *Nanotechnology* **2016**, *27*, 105702.
- (44) Grønberg, S. S.; Ulstrup, S.; Bianchi, M.; Dendzik, M.; Sanders, C. E.; Lauritsen, J. V.; Hofmann, P.; Miwa, J. A. Synthesis of Epitaxial Single-Layer MoS₂ on Au(111). *Langmuir* **2015**, *31*, 9700–9706.
- (45) Bollinger, M.; Lauritsen, J.; Jacobsen, K. W.; Nørskov, J. K.; Helveg, S.; Besenbacher, F. One-Dimensional Metallic Edge States in MoS₂. *Phys. Rev. Lett.* **2001**, *87*, 196803.
- (46) Guinier, A. *X-ray diffraction in crystals, imperfect crystals, and amorphous bodies*; Dover Publications, 1994.

- (47) El-Mahalawy, S.; Evans, B. The Thermal Expansion of 2H-MoS₂, 2H-MoSe₂ and 2H-WSe₂ between 20 and 800°C. *J. Appl. Cryst.* **1976**, *9*, 403–406.
- (48) Blanc, N.; Coraux, J.; Vo-Van, C.; N’Diaye, A. T.; Geaymond, O.; Renaud, G. Local Deformations and Incommensurability of High-Quality Epitaxial Graphene on a Weakly Interacting Transition Metal. *Phys. Rev. B* **2012**, *86*, 235439.
- (49) Martoccia, D.; Björck, M.; Schlepütz, C.; Brugger, T.; Pauli, S.; Patterson, B.; Greber, T.; Willmott, P. Graphene on Ru(0001): a Corrugated and Chiral Structure. *New J. Phys.* **2010**, *12*, 043028.
- (50) Martoccia, D.; Willmott, P.; Brugger, T.; Björck, M.; Günther, S.; Schlepütz, C.; Cervellino, A.; Pauli, S.; Patterson, B.; Marchini, S. et al. Graphene on Ru (0001): a 25× 25 Supercell. *Phys. Rev. Lett.* **2008**, *101*, 126102.
- (51) Robinson, I. K. Crystal Truncation Rods and Surface Roughness. *Phys. Rev. B* **1986**, *33*, 3830.
- (52) Warmuth, J.; Bruix, A.; Michiardi, M.; Hänke, T.; Bianchi, M.; Wiebe, J.; Wiesendanger, R.; Hammer, B.; Hofmann, P.; Khajetoorians, A. A. Band-Gap Engineering by Bi Intercalation of Graphene on Ir(111). *Phys. Rev. B* **2016**, *93*, 165437.
- (53) Huang, L. F.; Gong, P. L.; Zeng, Z. Correlation between Structure, Phonon Spectra, Thermal Expansion, and Thermomechanics of Single-Layer MoS₂. *Phys. Rev. B* **2014**, *90*, 045409.
- (54) Nix, F.; MacNair, D. The Thermal Expansion of Pure Metals: Copper, Gold, Aluminum, Nickel, and Iron. *Phys. Rev.* **1941**, *60*, 597.
- (55) Brumme, T.; Calandra, M.; Mauri, F. First-Principles Theory of Field-Effect Doping in Transition-Metal Dichalcogenides: Structural Properties, Electronic Structure, Hall Coefficient, and Electrical Conductivity. *Phys. Rev. B* **2015**, *91*, 155436.

- (56) Duerloo, K.-A. N.; Li, Y.; Reed, E. J. Structural Phase Transitions in Two-Dimensional Mo-and W-Dichalcogenide Monolayers. *Nat. Commun.* **2014**, *5*, 4214.
- (57) Tan, S. J. R.; Sarkar, S.; Zhao, X.; Luo, X.; Luo, Y. Z.; Poh, S. M.; Abdelwahab, I.; Zhou, W.; Venkatesan, T.; Chen, W. et al. Temperature- and Phase-Dependent Phonon Renormalization in $1T^{\prime}$ -MoS₂. *ACS Nano* **2018**, *12*, 5051–5058.
- (58) Andersen, A.; Kathmann, S. M.; Lilga, M. A.; Albrecht, K. O.; Hallen, R. T.; Mei, D. First-Principles Characterization of Potassium Intercalation in Hexagonal 2H-MoS₂. *J. Phys. Chem. C* **2012**, *116*, 1826–1832.
- (59) Martínez-Galera, A. J.; Schröder, U.; Huttmann, F.; Jolie, W.; Craes, F.; Busse, C.; Caciuc, V.; Atodiressei, N.; Blügel, S.; Michely, T. Oxygen Orders Differently Under Graphene: New Superstructures on Ir (111). *Nanoscale* **2016**, *8*, 1932–1943.
- (60) Somoano, R.; Hadek, V.; Rembaum, A. Alkali Metal Intercalates of Molybdenum Disulfide. *J. Chem. Phys.* **1973**, *58*, 697–701.
- (61) Lindgren, S.; Walldén, L. Photoemission of Electrons at the Cu(111)/Na Interface. *Solid State Commun.* **1980**, *34*, 671–673.
- (62) Forster, F.; Bendounan, A.; Ziroff, J.; Reinert, F. Systematic Studies on Surface Modifications by ARUPS on Shockley-Type Surface States. *Surf. Sci.* **2006**, *600*, 3870–3874.
- (63) Miwa, J. A.; Ulstrup, S.; Sørensen, S. G.; Dendzik, M.; Čabo, A. G.; Bianchi, M.; Lauritsen, J. V.; Hofmann, P. Electronic Structure of Epitaxial Single-Layer MoS₂. *Phys. Rev. Lett.* **2015**, *114*, 046802.